

# Universal preference for low-energy core-shifted grain boundaries at the surfaces of fcc metals

Xiaopu Zhang<sup>✉\*</sup> and John J. Boland<sup>†</sup>

Centre for Research on Adaptive Nanostructures and Nanodevices (CRANN), AMBER SFI Research Centre and School of Chemistry, Trinity College Dublin, Dublin 2, Ireland



(Received 2 November 2022; accepted 2 March 2023; published 31 March 2023)

Grain boundaries (GBs) with [111] tilt axes are common in polycrystalline face-centered cubic (fcc) metals. For copper (111) films, emergent GBs close to the surface have tilt axes that are shifted away from [111] that are lower in energy than the corresponding truncated bulk boundaries. Geometrical analysis and atomic calculations were used to study the driving force for this same relaxation phenomenon in representative fcc elemental metals. We show that the reduction in boundary energy scales with the elimination of energetically costly boundary core facets. We find that, for a wide range of misorientation angles, low-energy core-shifted boundaries are also favored in Al, Ni, Au, and Pt and discuss the significance for electromigration and other metal properties.

DOI: [10.1103/PhysRevResearch.5.013223](https://doi.org/10.1103/PhysRevResearch.5.013223)

## I. INTRODUCTION

The structure and stability of grain boundary (GB) defects at surfaces and interfaces control material properties such as corrosion, catalysis, and mechanical strength [1–8]. The defect or reduced binding energy relative to the bulk is responsible for electromigration-induced failure at GBs in metals [9]. While strategies to stabilize GBs via the dopant incorporation have been developed, we recently showed that it is possible to generate anomalously stable boundaries at the surfaces of nanoscale polycrystalline copper (111) films and bicrystals [10–12]. Experiments show these emergent GBs (eGBs) have tilt axes that are locally shifted away from [111], which are made possible by an out-of-plane rotation of the adjoining grains [11]. Simulations revealed a significant reduction (~20%) in the boundary energy and the formation of structures with boundary cores that lie along close-packed planes. Small out-of-plane rotations lead to significant reductions in the boundary energy. The balance between boundary-energy reduction and the elastic energy cost due to grain rotation determines the depth of the low-energy core-shifted boundary (CSB) [11]. For copper, CSBs can extend to many nanometers beneath the surface, approaching the dimensions of current metal interconnect technologies [13]. The formation of CSBs in the near surface region is facilitated by the increased capacity for relaxation at free surfaces. However, it remains to be established whether it is possible to engineer CSBs over larger length scales.

In this paper, we show that this same GB relaxation phenomenon occurs in other face-centered cubic (fcc) metals, and we determine the degree of energy stabilization and the length scales of the CSBs in each case. To do so, we developed a generalized methodology to calculate the change in boundary geometric structure during the relaxation process. We considered symmetric [111] tilt boundaries with in-plane misorientation angle  $\theta$  and a  $(1\bar{1}0)$  mean boundary plane. We calculated the boundary energy as a function of the angular shift of the combined rotation axis (CRA)—due to combining the in-plane and out-of-plane rotations—along the trajectory from the original [111] tilt axis of the film [as it shifts across the  $(1\bar{1}0)$  boundary plane] toward [112], which lies in the  $[11\bar{1}]$  close-packed plane. We then elucidated the relationship between structure change and the change in the boundary energy. Our analyses clearly show that CSBs are energetically preferred in fcc elemental metals, and we discuss the origin of this behavior and its wider importance.

## II. BICRYSTAL GEOMETRY WITH/O OUT-OF-PLANE ROTATION

We begin by constructing, in the  $xyz$  coordinate system, the reference lattice from a perfect fcc lattice with its orientation  $x \parallel [\bar{1}\bar{1}2]$ ,  $y \parallel [1\bar{1}0]$ , and  $z \parallel [111]$ , as shown in Fig. 1(a). Then the black and white lattices are generated by rotating the reference lattice by  $\pm\theta/2$  along the rotation axis [111], respectively, where  $\theta$  is the in-plane misorientation angle. To create the bicrystal, we choose the  $xz$  plane as the boundary plane, keeping the upper half of the black lattice and similarly keeping the lower half of the white lattice [see Fig. 1(b)]. This process creates a symmetric tilt GB with tilt axis [111], misorientation angle  $\theta$ , mean period vector  $[\bar{1}\bar{1}2]$ , and mean boundary plane  $(1\bar{1}0)$ . If the axis of the symmetrical tilt GBs is along vector  $e_3 = [111]$ , the mean period vector direction is along vector  $e_1 = \frac{1}{4}[\bar{1}\bar{1}2]$ , and the Burgers vector direction is along vector  $e_2 = \frac{1}{4}[1\bar{1}0]$ . The mean period vector can be written as  $\vec{q} = ke_1$ , and the half

\*xiaopuz@tcd.ie

†jboland@tcd.ie

Published by the American Physical Society under the terms of the Creative Commons Attribution 4.0 International license. Further distribution of this work must maintain attribution to the author(s) and the published article's title, journal citation, and DOI.

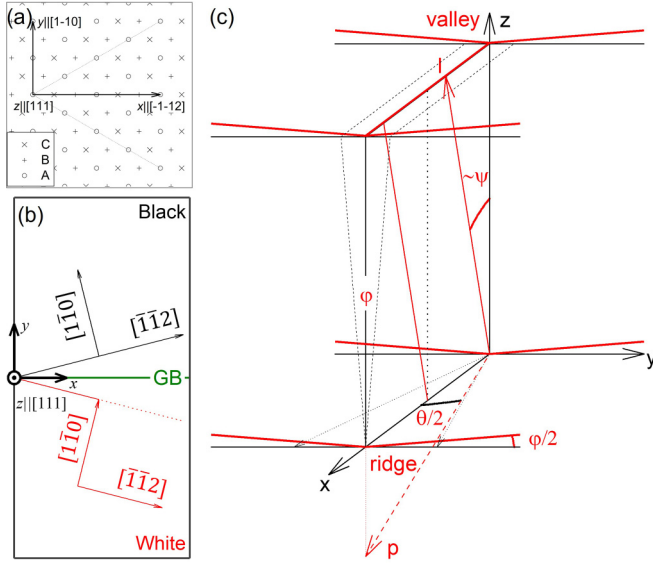


FIG. 1. Boundary geometry. (a) Reference lattice adhering to the  $xyz$  coordination system. (b) Bicrystals and their own coordination system. (c) Out-of-plane rotation  $\phi$ , the combined rotation axis (CRA)  $l$ , and the new period vector  $p$  in the new bicrystal.

Burger vector is  $\vec{B}/2 = le_2$ , where  $k$  and  $l$  are integers. The period vectors in the white and black crystals are then written as follows, respectively:  $p_b = \vec{q} - \vec{B}/2 = ke_1 - le_2 = \frac{1}{4}[-k-l, -k+l, 2k]$  and  $p_w = \vec{q} + \vec{B}/2 = ke_1 + le_2 = \frac{1}{4}[-k+l, -k-l, 2k]$ , where  $\frac{1}{2}[\bar{1}\bar{1}2]$  and  $\frac{1}{2}[1\bar{1}0]$  are shortest lattice vectors along their corresponding directions. Since the Burgers vector is  $p_w - p_b = l \cdot \frac{1}{2}[1\bar{1}0]$ ,  $l$  with integer values represents full dislocations. This implies that there are  $l$  full Burgers vectors every  $k/4 [\bar{1}\bar{1}2]$  spacing. Note that, if  $k \pm l$  are even integers, the period vector is a lattice vector. Otherwise, two times this distance is taken as the period vector. The misorientation angle is then given by Frank's formula in the form below [14]  $\tan(\theta/2) = l/(\sqrt{3}k)$ . Using the surface basis of  $\frac{1}{4}[\bar{1}\bar{1}2]$  and  $\frac{1}{4}[1\bar{1}0]$ , the period vector can be rewritten as  $[k, l]$  in surface notation [11]. The reciprocal density of coincidence sites  $\Sigma$  is calculated as  $\Sigma = (3k)^2 + (\sqrt{3}l)^2$  with any factors of 2 canceled out [15]. The GB normal is along  $\vec{e}_3 \times \vec{p} \propto [111] \times \vec{p}$ . For the white and black crystals,

respectively, the boundary normals are  $\vec{n}_b = \frac{1}{4}[3k-l, -3k-l, 2l]$  and  $\vec{n}_w = \frac{1}{4}[3k+l, -3k+l, -2l]$ . Selected geometrical parameters are listed in Table I.

To include out-of-plane rotation, we further rotate the black and white lattices by  $\pm\phi/2$  along the  $x$  axis, respectively. The bicrystals before and after the out-of-plane rotation are shown as black and red in Fig. 1(c). The CRA (also the direction of boundary cores) is still in the  $xz$  plane, shown in red. Note that the out-of-plane rotation axis is also in the boundary plane and parallel to the valley or ridge on the top and bottom, respectively. The resulting inclination angle  $\psi$ , shown in Fig. 1(c), is the angle between  $[111]$  in the bicrystal after the out-of-plane rotation and the CRA. From the two vectors in the boundary plane, the out-of-plane rotation axis and the CRA, the boundary normal is calculated. Then we calculated a new period vector of the bicrystal from the cross-product of the CRA and the boundary normal. The geometry specifications for the boundaries with in-plane angle  $\theta = 26.01^\circ$  (GB26.01) with different CRAs, together with the corresponding inclination angles, are listed in Table II. This method leads to much smaller unit cell sizes, making massive calculations feasible, compared with the linear combination method in our previous paper [10]. Taking the boundary with the in-plane angle  $\theta = 3.89^\circ$  and out-of-plane angle  $0.79^\circ$  as an example, the boundary normal is  $[58 \ 61 \ 2]$ . In our previous analysis, the period vector is  $[\bar{9} \ 817]$ , and the rotation axis is  $[1021 \ 1004 \ 1013]$  [10]. Using the present approach based on the minimum unit cell, the two vectors are  $[223]$  (the direction of boundary cores) and  $[187 \ 170 \ 238]$ . The boundary area and cell volume in each cell are then  $\sim 25$  times smaller.

### III. INCLINATION ANGLE-DEPENDENT BOUNDARY ENERGY AND STRUCTURE

We calculated the boundary energies in the bulk for a range of fcc metals as a function of the inclination angle of the CRA away from  $[111]$  for different misorientation angles. In all cases, the mean boundary planes are in the  $(\bar{1}\bar{1}0)$  plane. Boundaries were calculated with LAMMPS software, the molecular statics method, and the widely used embedded-atom method (EAM) interatomic potentials for Cu, Ni, Al, Au, and Pt [16–18]. To explore the effect of different potentials, we used the third-generation charge-optimized many-body (COMB3) potential for Pt, to capture the effects of its high

TABLE I.  $[111]$  ST-GB with mean boundary plane  $(\bar{1}\bar{1}0)$  and mean period vector  $[\bar{1}\bar{1}2]$ .

$[k, l]$	$\tan \frac{\theta}{2}$	$\theta(^{\circ})$	$\Sigma$	Period vectors black–white	Boundary normal black–white
[1,1]	$1/\sqrt{3}$	60.00	3	$\frac{1}{2}[\bar{1}01] \ \frac{1}{2}[0\bar{1}1]$	$\frac{1}{2}[2\bar{1}\bar{1}] \ \frac{1}{2}[1\bar{1}2]$
[2,1]/[4,2]	$1/2\sqrt{3}$	32.20	39	$\frac{1}{2}[\bar{3}\bar{1}4] \ \frac{1}{2}[\bar{1}\bar{3}4]$	$\frac{1}{2}[5\bar{7}2] \ \frac{1}{2}[7\bar{5}\bar{2}]$
[5,2]/[10,4]	$2/5\sqrt{3}$	26.01	237	$\frac{1}{2}[\bar{7}\bar{3}10] \ \frac{1}{2}[\bar{3}\bar{7}10]$	$\frac{1}{2}[13\bar{1}74] \ \frac{1}{2}[17\bar{1}3 \ 4]$
[3,1]	$1/3\sqrt{3}$	21.79	21	$\frac{1}{2}[\bar{2}\bar{1}3] \ \frac{1}{2}[\bar{1}\bar{2}3]$	$\frac{1}{2}[4\bar{5}1] \ \frac{1}{2}[5\bar{4}\bar{1}]$
[5,1]	$1/5\sqrt{3}$	13.17	57	$\frac{1}{2}[\bar{3}\bar{2}5] \ \frac{1}{2}[\bar{2}\bar{3}5]$	$\frac{1}{2}[7\bar{8}1] \ \frac{1}{2}[8\bar{7}\bar{1}]$
[17,1]	$1/17\sqrt{3}$	3.89	651	$\frac{1}{2}[\bar{9}\bar{8}17] \ \frac{1}{2}[\bar{8}\bar{9}17]$	$\frac{1}{2}[25 \ 26 \ 1] \ \frac{1}{2}[26 \ 25 \ \bar{1}]$

TABLE II. Geometrical specification of GB [111] 26.01 with different composite rotation axis.

Composite axis $l$	$\psi$ ( $^\circ$ )	Boundary normal black-white	Period vector black-white
[552]	-19.47	[14 $\bar{16}$ 5] [16 $\bar{14}$ $\bar{5}$ ]	$[\bar{19}$ $\bar{1}$ 50] [ $\bar{1}$ $\bar{19}$ 50]
[221]	-15.79	[23 $\bar{27}$ 8] [27 $\bar{23}$ $\bar{8}$ ]	$[\bar{43}$ $\bar{7}$ 100] [ $\bar{7}$ $\bar{43}$ 100]
[332]	-10.02	[9 $\bar{11}$ 3] [11 $\bar{9}$ $\bar{3}$ ]	$[\bar{31}$ $\bar{9}$ 60] [ $\bar{9}$ $\bar{31}$ 60]
[111]	0	[13 $\bar{17}$ 4] [17 $\bar{13}$ $\bar{4}$ ]	$[\bar{73}$ 10] [ $\bar{37}$ 10]
[334]	8.05	[21 $\bar{29}$ 6] [29 $\bar{21}$ $\bar{6}$ ]	$[\bar{67}$ $\bar{33}$ 75] [ $\bar{33}$ $\bar{67}$ 75]
[223]	11.42	[29 $\bar{41}$ 8] [41 $\bar{29}$ $\bar{8}$ ]	$[\bar{139}$ $\bar{71}$ 140] [ $\bar{71}$ $\bar{139}$ 140]
[335]	14.42	[45 $\bar{65}$ 12] [65 $\bar{45}$ $\bar{12}$ ]	$[\bar{361}$ $\bar{189}$ 330] [ $\bar{189}$ $\bar{361}$ 330]
[112]	19.47	[4 $\bar{6}$ 1] [6 $\bar{4}$ $\bar{1}$ ]	$[\bar{13}$ $\bar{7}$ 10] [ $\bar{7}$ $\bar{13}$ 10]
[225]	25.24	[35 $\bar{55}$ 8] [55 $\bar{35}$ $\bar{8}$ ]	$[\bar{97}$ $\bar{53}$ 60] [ $\bar{53}$ $\bar{97}$ 60]
[113]	29.50	[19 $\bar{31}$ 4] [31 $\bar{19}$ $\bar{4}$ ]	$[\bar{97}$ $\bar{53}$ 50] [ $\bar{53}$ $\bar{97}$ 50]

stacking faulting energy [19–21]. We built each repeat cell with a pair of parallel GBs of equal and opposite misorientation and used periodic boundary conditions in three directions [16,19,22]. Fully relaxed configurations were obtained by energy minimization with respect to both the atomic coordinates and the cell size along the boundary normal via a conjugate-gradient method. Structure searching with hundreds of initial configurations with different relative displacements parallel to the boundary plane was performed, and only the lowest energy structures are reported in this paper [23]. Considering the threefold inversion symmetry of the [111] tilt axis in fcc lattices, only boundaries with misorientations from  $0^\circ$  to  $60^\circ$  are considered [24].

Results for misorientation angles between  $0^\circ$  and  $32.20^\circ$  are shown in Figs. 2(a)–2(f), with higher angle boundaries shown in Figs. 2(g)–2(l). The misorientation angle  $32.20^\circ$  corresponds to the boundary [2,1] in surface notation, which has one full dislocation every two  $[1\bar{1}0]$ -atomic-line spacings in the Burgers vector loop. For all calculated fcc metals, the boundary energy increases monotonically with the in-plane angle from  $0^\circ$  to  $\sim 32.20^\circ$ . Boundaries with [112] tilt axis ( $\psi = 19.47^\circ$ ) are always lowest in energy, and the boundary energy decreases nearly linearly as the CRA shifts from [111] toward [112], i.e., CSBs with a [112] tilt axis are a global energy minimum regardless of the direction of the original tilt axis. The same trends are clearly seen for Pt in Figs. 2(e)–2(f) regardless of whether the EAM or COMB3 potentials were employed. These results indicate that CSBs with [112] tilt axes in fcc metals are energetically preferred, and there is no thermodynamic barrier to grain rotation. Figures 2(g)–2(l) show the inclination-dependent boundary energy with in-plane misorientation angles above  $32.20^\circ$ . We find that boundaries with [112] tilt axis are still preferred energetically. However, the transition is neither linear nor smooth. For example, the dependence for GB38.21 shows a barrier between [111] and [112]. Moreover, at negative inclination angles, the inclination energy dependences are no longer monotonic.

Figure 3(a) visualizes the core structure for GB26.01 with different inclination angles and the corresponding boundary energies ( $\text{mJ m}^{-2}$ ). The length along the CRA shown in each case is three times that of the vector shown in red below each panel. The boundary cores facet into segments along

[112] that lie in the close-packed  $(11\bar{1})$  plane and evenly distributed  $\frac{1}{2}[110]$  segments that lie out of the plane, indicated by red arrows [25]. The CRA shift toward [112] reduces the boundary energy and, at the same time, reduces and eventually eliminates these energetically unfavorable jogs within the boundary core. For low-angle boundaries, the segments along [112] prefer to dissociate into stacking fault ribbons that are a balance between decreasing the repulsive interactions between partials and minimizing the stacking fault area and energy [26]. On the other hand, each  $\frac{1}{2}[110]$  segment is essentially a jog within the boundary core, shifting one stacking fault ribbon into a neighboring slip plane, and in doing so, it constrains the stacking fault dissociation and hence increases the total dislocation line energy.

To establish the relationship between changes in GB structure and energy, we analyzed the energy variation and the density of jogs at several inclination angles. We write, according to our calculated structures, the CRA vector or the effective boundary core direction as  $n/2[112] + \frac{1}{2}[110]$  with content:

$$l = \frac{\sqrt{(n+1)^2 + 2n^2}}{\sqrt{2}}, \quad (1)$$

where  $n \geq 1$  and positive integers are taken in our atomic calculation. For example,  $n = 1$  corresponds to [111],  $n = 2$  to [334],  $n = 3$  to [223],  $n = 5$  to [335], and  $n = \infty$  to [112]. For a given value of  $n$ , the calculated jog line density, which is the number of jogs per unit length, is

$$\rho_l = \frac{1}{la}, \quad (2)$$

and the inclination angle is

$$\cos\psi = \frac{2n+1}{\sqrt{3}l} \quad (3)$$

where  $a$  is the lattice constant. During the out-of-plane rotation process, the initial spacing between two boundary cores is changed since, for any given boundary area, the dislocation line length varies as  $1/\cos\psi$ , which is  $\sim 1$ , since the angle  $\psi$  is small. Our analysis in Fig. 3(b) shows that the boundary

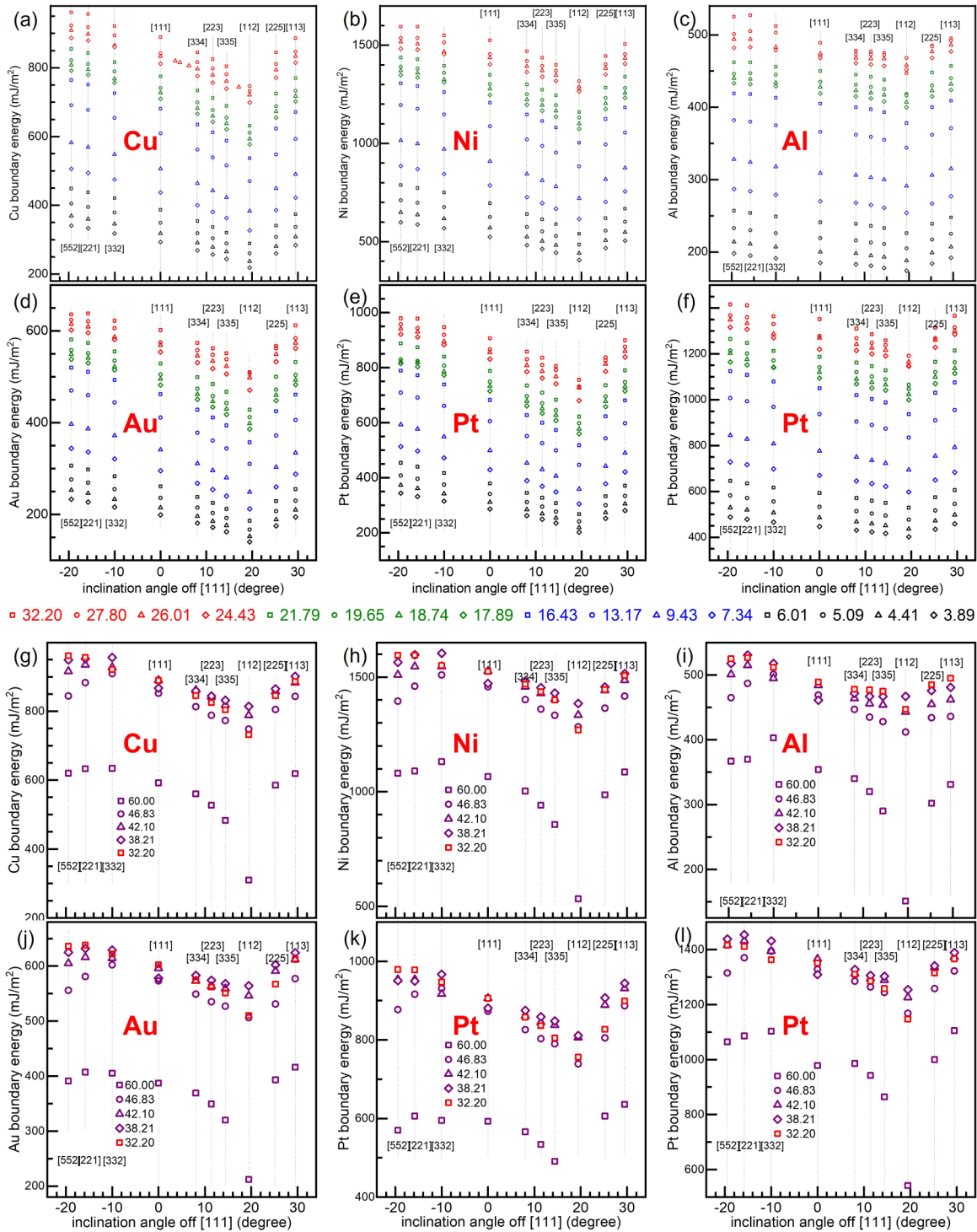


FIG. 2. Inclination angle-dependent grain boundary (GB) energy for different face-centered cubic (fcc) metal with misorientation angles from 0 to 32.20 for (a) copper, (b) nickel, (c) aluminum, (d) gold, (e) platinum with EAM potential, and (f) platinum with COMB3 potential. Inclination angle dependent GB energy for different fcc metal with misorientation angles from 32.20 to 60.00 for (g) copper, (h) nickel, (i) aluminum, (j) gold, (k) platinum with embedded-atom method (EAM) potential, and (l) platinum with charge-optimized many-body (COMB) potential.

energy variation is nearly proportional to the jog density (the jog number per unit area) so that

$$\Delta\gamma \propto \frac{\sqrt{3}}{2n + 1} \quad (4)$$

The proportional coefficients (standard error) from Fig. 3(b) for GB3.89 and GB26.01 in copper are 136(5) and 209(9), respectively. This excellent scaling suggests that the interaction between jogs both within and between cores is small. The standard error is <5% of the slope for calculated boundaries

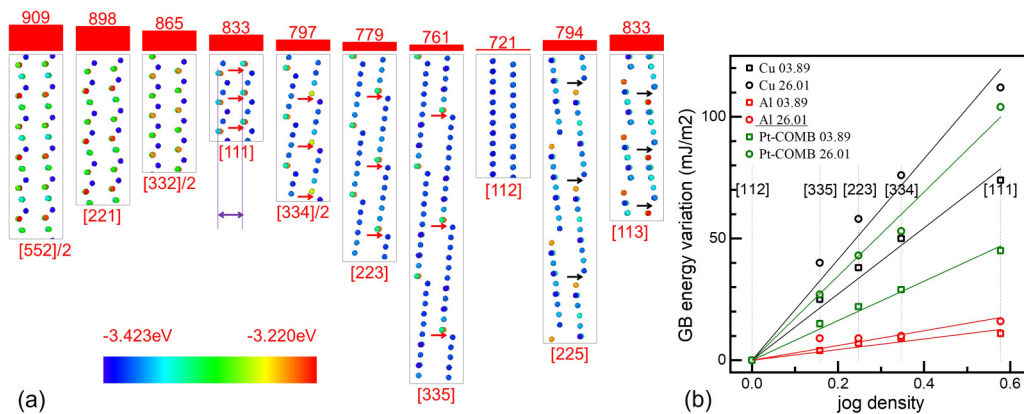


FIG. 3. Relationship between grain boundary (GB) energy variation and the jog density. (a) Change of the boundary cores with in-plane angle  $26.01^\circ$  at different tilt axes in the  $(1\bar{1}0)$  plane, with histogram of the boundary energy ( $\text{mJ m}^{-2}$ ). The boundaries are viewed along the  $x$  direction shown in Fig. 1(c). The length along the tilt axis is three times the vector below each graph. Atoms are colored by energy, and the arrows point to jogs. (b) Plot of GB energy variation and the jog density.

with different misorientation angles in all metals, except for high-angle boundaries in Pt and Al. For Pt using the COMB3 potential and Al with EAM potential, our calculated stacking fault energies ( $321$  and  $146 \text{ mJ/m}^2$ , respectively) are high, preventing relaxation of the stresses within the cores and hence the presence of long-range elastic interactions among jogs and neighboring cores [17,21]. As the CRA shifts in the  $(1\bar{1}0)$  plane from  $[110]$  toward  $[111]$  ( $\psi < 0$  in Fig. 2), the  $\frac{1}{2}[110]$  segments are close to each other, and the dependence shifts away from being proportional since their interaction must then be considered. As the CRA shifts from  $[112]$  toward  $[001]$  with  $\psi > 19.47^\circ$ , different segments or jogs are now involved, highlighted in Fig. 3(a) using black arrows, and hence, different coefficients are expected.

#### IV. MISORIENTATION DEPENDENT ENERGY VARIATION AND RESTRUCTURING DEPTH

The linear relationship in Fig. 3(b) clearly shows that the energy reduction that drives CSB formation is achieved through removing energetically unfavorable boundary-core facets, i.e., a preference for boundary cores to lie along close-packed planes. The normalized ratios of the CSB energy variation compared with that of the original  $[111]$  boundaries are shown in Fig. 4. For copper, nickel, and gold, the energy reduction ranges from  $\sim 30\%$  at low-angle boundaries and decreases to  $\sim 10\%$  before increasing to  $>40\%$  for GB60 twin boundaries. The corresponding ratios for aluminum are reduced, while the behavior of platinum depends on potential used, consistent with higher stacking fault energies and a

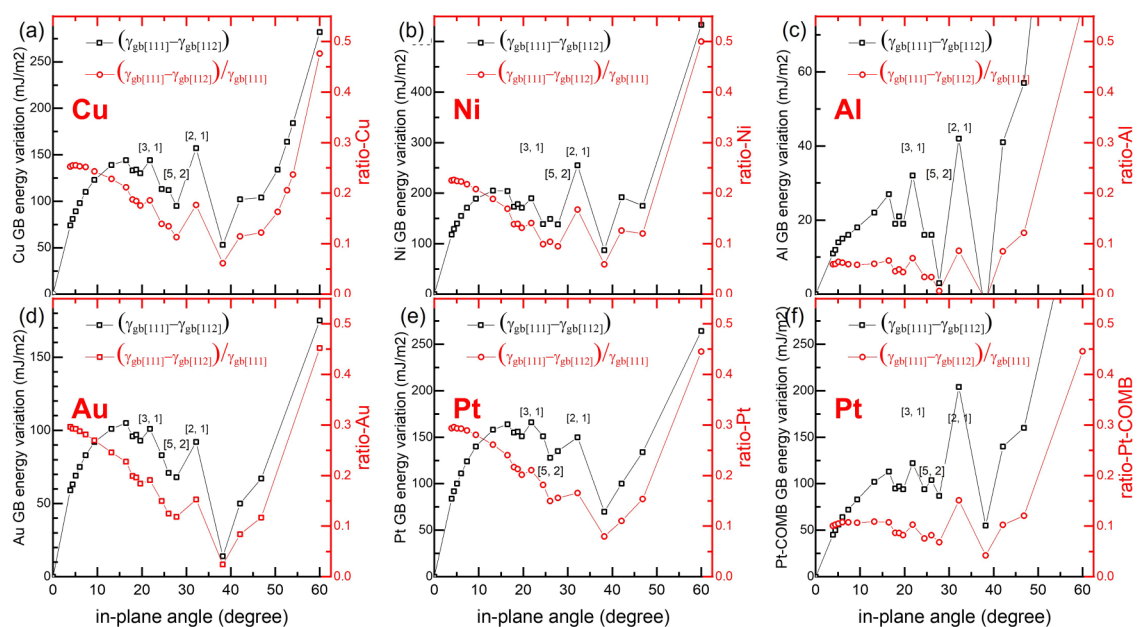


FIG. 4. Misorientation-dependent grain boundary (GB) energy variation and their ratio for (a) copper, (b) nickel, (c) aluminum, (d) gold, (e) platinum with embedded-atom method (EAM) potential, and (f) platinum with charge-optimized many-body (COMB) potential.

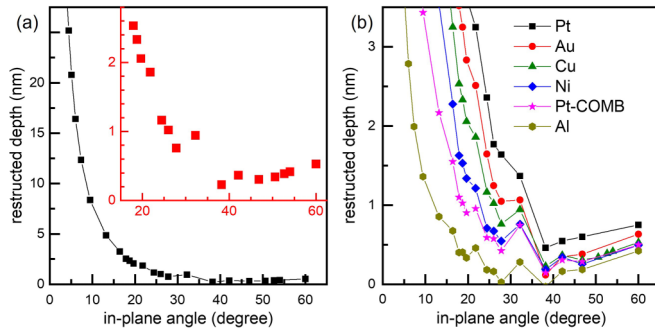


FIG. 5. Misorientation-dependent restructuring depth. (a) Dots and line show the misorientation angle-dependent restructuring depth. (b) The same dependence for all calculated face-centered cubic (fcc) metals.

reduced stabilization of dissociated boundary cores (see Fig. 4). In all cases, simulations predict an energy stabilization that is particularly significant for low-angle boundaries.

Figure 4 shows the boundary energy difference for different metals and their normalized ratios, defined as the energy difference divided by the energy of the original boundary with [111] tilt axis. For all metals, the energy difference is seen to increase with the in-plane angle up to  $16.43^\circ$ , corresponding to the boundary [4, 1]. At higher misorientation angles, there are three main peaks located at  $21.79^\circ$  for boundary [3, 1],  $32.20^\circ$  for boundary [2, 1], and  $60^\circ$  for boundary [1, 1]. These peaks are at boundaries with lower geometrical parameters  $k = 1, 2, 3$  and  $l = 1$ , rather than those with low  $\Sigma$ , which in essence describes the lattice properties. In addition, we find that there are smaller peaks among the  $l = 1$  peaks, which correspond to  $l = 2$  at different  $k = 3, 5, 7$ . We note that the level of hierarchy related to the delimiting boundary was previously discussed in the structure unit model of GBs [27, 28]. We attribute this similarity to the boundary geometry that both analyses are based on. In contrast with the energy difference, the variation in the normalized ratio in Fig. 4 decreases with the in-plane angle up to  $16.43^\circ$ . It also shows  $l$  hierarchical related oscillations that range from 10% to 25% for in-plane angles  $< 32.20^\circ$ . We note that the normalized ratio for aluminum is  $\sim 5\%$  and that for Pt using the COMB potential  $\sim 10\%$ , which are smaller than for other fcc metals and for Pt using the EAM potential (see Fig. 4).

To estimate the extended depth of CSBs beneath the surface, we calculated the energy difference  $\Delta\gamma_{gb}$  between a bulk GB with a tilt axis [111] and its corresponding bulk boundary with its CRA shifted to [112]. We then estimated the CSB depth  $h$  as

$$h = \frac{\Delta\gamma_{gb}}{2cG\varphi^2} \quad (5)$$

by balancing the energetic driving force  $-\Delta\gamma_{gb} \cdot h$  and the elastic energy cost  $c \cdot G\varphi^2 h^2$ , where  $\varphi$  is the out-of-plane angle, the coefficient  $c$  is related to Poisson ratio, and  $G$  is the shear modulus [11]. Figure 5(a) shows a plot of the CSB depth  $h$  for copper as a function of the misorientation angle with  $cG = 4.35$  GPa. A close-up view of the plot with

misorientation angle  $> 15^\circ$  is shown as an inset. Clearly, while the CSB depth can be many nanometers for low-angle boundaries, it decreases with misorientation angle and is ultimately reduced to atomic layer thicknesses beyond  $\sim 32.20^\circ$ . At higher angles, while there is a modest increase in the CSB depth, it is still limited to several atomic layers, so it remains a surface effect.

The CSB depth for other fcc metals shown in Fig. 5(b) was estimated neglecting the misorientation-related elastic anisotropy. The same value  $c$  was used for all metals, and the value for  $G$  along the metal (111) plane was obtained using elastic parameters calculated for each metal [29, 30]. We see from Fig. 5(b) that the variation of the CSB depth with misorientation angle is like that found in copper. The transition from a many-nanometer scale tilted boundary to a surface effect still occurs at misorientation angle of  $\sim 30^\circ$ . The notable exception is Al, where the variation ratio of the boundary energy is reduced [see Fig. 4(c)], and hence, the curve is uniformly shifted to reduced depths so that, in this case, the transition occurs at  $\sim 20^\circ$ . Recognizing that the distribution of GBs in polycrystalline and nanocrystalline materials is inversely correlated with the boundary energy [31], the predominance of lower angle GBs suggests that most of the emergent boundaries at the free surfaces of fcc metals are CSBs with depths of several to many nanometers. Moreover, since these dominant low-angle CSBs also exhibit the greatest level of energy stabilization (see Fig. 4), there is significant potential to mitigate against electromigration in metals by optimizing GB structure.

## V. CONCLUSIONS

In summary, our geometrical analysis and calculations show that CSB formation is driven by the systematic removal of energetically unfavorable boundary-core facets that ultimately results in eGB with cores that lie along close-packed planes. Even small levels of boundary tilting result in significant reductions in boundary energy. The energy stabilization is significant for all fcc metals, regardless of the material differences, elastic constants, and stacking fault energies. Collectively, these results demonstrate that the elimination of core facets is a fundamental thermodynamic principle that drives CSB formation at the free surfaces of all fcc materials. The core-shifting phenomenon is expected to be particularly important for nanoscale metals since the CSB depth approaches the physical dimensions of these materials. In addition to electromigration, eGB structure and stability are known to impact a wide range of phenomena—grain coalescence and thin film formation, mechanical strength, electrical conductivity, and catalytic activity [1, 3, 4, 32–38]—so that additional research is needed to elucidate the role of CSBs in controlling metal properties and performance on the nanoscale [38].

## ACKNOWLEDGMENTS

J.J.B. and X.Z. acknowledge support from Science Foundation Ireland (Grants No. 12/RC/2278 and No. 16/IA/4462) and thank Trinity Centre for High Performance for providing the computing. X.Z. thanks Urvesh Patil for technical support.

- [1] Y.-Y. Zhang, H. Xie, L.-Z. Liu, and H.-J. Jin, Surface Triple Junctions Govern the Strength of a Nanoscale Solid, *Phys. Rev. Lett.* **126**, 235501, (2021).
- [2] X. Zhao, T. K. Gunji, F. Lv, B. L. Huang, R. Ding, J. G. Liu, M. C. Luo, Z. G. Zou, and S. J. Guo, Direct observation of heterogeneous surface reactivity and reconstruction on terminations of grain boundaries of platinum, *ACS Mater. Lett.* **3**, 622 (2021).
- [3] H. Bishara, S. Lee, T. Brink, M. Ghidelli, and G. Dehm, Understanding grain boundary electrical resistivity in Cu: The effect of boundary structure, *ACS Nano* **15**, 16607 (2021).
- [4] D. An, T. A. Griffiths, P. Konijnenberg, S. Mandal, Z. Wang, and S. Zaeferrer, Correlating the five parameter grain boundary character distribution and the intergranular corrosion behaviour of a stainless steel using 3D orientation microscopy based on mechanical polishing serial sectioning, *Acta Mater.* **156**, 297 (2018).
- [5] C. Wang, K. Du, K. Song, X. Ye, L. Qi, S. He, D. Tang, N. Lu, H. Jin, F. Li *et al.*, Size-Dependent Grain-Boundary Structure with Improved Conductive and Mechanical Stabilities in Sub-10-nm Gold Crystals, *Phys. Rev. Lett.* **120**, 186102 (2018).
- [6] C. W. Li, J. Ciston, and M. W. Kanan, Electroreduction of carbon monoxide to liquid fuel on oxide-derived nanocrystalline copper, *Nature (London)* **508**, 504 (2014).
- [7] R. G. Mariano, K. McKelvey, H. S. White, and M. W. Kanan, Selective increase in CO<sub>2</sub> electroreduction activity at grain-boundary surface terminations, *Science* **358**, 1187 (2017).
- [8] B. Wu, A. Heidelberg, J. J. Boland, J. E. Sader, X. Sun, and Y. Li, Microstructure-hardened silver nanowires, *Nano Lett.* **6**, 468 (2006).
- [9] K. C. Chen, W. W. Wu, C. N. Liao, L. J. Chen, and K. N. Tu, Observation of atomic diffusion at twin-modified grain boundaries in copper, *Science* **321**, 1066 (2008).
- [10] X. Zhang, J. Han, J. J. Plombon, A. P. Sutton, D. J. Srolovitz, and J. J. Boland, Nanocrystalline copper films are never flat, *Science* **357**, 397 (2017).
- [11] X. Zhang, M. Wang, H. Wang, M. Upmanyu, and J. J. Boland, Restructuring of emergent grain boundaries at free surfaces—An interplay between core stabilization and elastic stress generation, *Acta Mater.* **242**, 118432, (2023).
- [12] J. Schiotz and K. W. Jacobsen, Nanocrystalline metals: Roughness in flatland, *Nat. Mater.* **16**, 1059 (2017).
- [13] B. Sell, S. An, J. Armstrong, D. Bahr, B. Bains, R. Bambery, K. Bang, D. Basu, S. Bendapudi, D. Bergstrom *et al.*, Intel 4 CMOS technology featuring advanced FinFET transistors optimized for high density and high-performance computing, in *Proceedings of the 2022 IEEE Symposium on VLSI Technology and Circuits* (IEEE, Piscataway, NJ, 2022), pp. 282–283.
- [14] J. W. Christian, *The Theory of Transformations in Metals and Alloys* (Elsevier Science, Oxford, 2002).
- [15] A. P. Sutton and R. W. Balluffi, *Interfaces in Crystalline Materials* (Oxford University Press, Oxford, 2006).
- [16] Y. Mishin, M. J. Mehl, D. A. Papaconstantopoulos, A. F. Voter, and J. D. Kress, Structural stability and lattice defects in copper: *Ab initio*, tight-binding, and embedded-atom calculations, *Phys. Rev. B* **63**, 224106 (2001).
- [17] Y. Mishin, D. Farkas, M. J. Mehl, and D. A. Papaconstantopoulos, Interatomic potentials for monoatomic metals from experimental data and *ab initio* calculations, *Phys. Rev. B* **59**, 3393 (1999).
- [18] S. M. Foiles, M. I. Baskes, and M. S. Daw, Embedded-atom-method functions for the fcc metals Cu, Ag, Au, Ni, Pd, Pt, and their alloys, *Phys. Rev. B* **33**, 7983 (1986).
- [19] S. Plimpton, Fast parallel algorithms for short-range molecular-dynamics, *J. Comput. Phys.* **117**, 1 (1995).
- [20] T. Liang, T. R. Shan, Y. T. Cheng, B. D. Devine, M. Noordhoek, Y. Z. Li, Z. Z. Lu, S. R. Phillpot, and S. B. Sinnott, Classical atomistic simulations of surfaces and heterogeneous interfaces with the charge-optimized many body (COMB) potentials, *Mater. Sci. Eng. R* **74**, 255 (2013).
- [21] A. C. Antony, S. A. Akhade, Z. Lu, T. Liang, M. J. Janik, S. R. Phillpot, and S. B. Sinnott, Charge optimized many body (COMB) potentials for Pt and Au, *J. Phys.: Condens. Matter* **29**, 225901 (2017).
- [22] M. A. Tschopp and D. L. McDowell, Asymmetric tilt grain boundary structure and energy in copper and aluminium, *Philos. Mag.* **87**, 3871 (2007).
- [23] J. Han, V. Vitek, and D. J. Srolovitz, Grain-boundary metastability and its statistical properties, *Acta Mater.* **104**, 259 (2016).
- [24] G. J. Wang, A. P. Sutton, and V. Vitek, A computer-simulation study of (001) and (111) tilt boundaries—The multiplicity of structures, *Acta Metall.* **32**, 1093 (1984).
- [25] A. Stukowski, Visualization and analysis of atomistic simulation data with OVITO—The Open Visualization Tool, *Modelling Simul. Mater. Sci. Eng.* **18**, 015012 (2010).
- [26] P. M. Anderson, J. P. Hirth, and J. Lothe, *Theory of Dislocations* (McGraw-Hill, New York, 1967).
- [27] J. Han, V. Vitek, and D. J. Srolovitz, The grain-boundary structural unit model redux, *Acta Mater.* **133**, 186 (2017).
- [28] A. P. Sutton and V. Vitek, On the structure of tilt grain boundaries in cubic metals I. Symmetrical tilt boundaries, *Philos. Trans. Royal Soc. A* **309**, 1 (1983).
- [29] J. F. Nye, *Physical Properties of Crystals: Their Representation by Tensors and Matrices* (Clarendon Press, Oxford, 1985).
- [30] A. Marmier, Z. A. D. Lethbridge, R. I. Walton, C. W. Smith, S. C. Parker, and K. E. Evans, EIAM: A computer program for the analysis and representation of anisotropic elastic properties, *Comput. Phys. Commun.* **181**, 2102 (2010).
- [31] G. S. Rohrer, Grain boundary energy anisotropy: A review, *J. Mater. Sci.* **46**, 5881 (2011).
- [32] X. W. Gu, C. N. Loynachan, Z. Wu, Y. W. Zhang, D. J. Srolovitz, and J. R. Greer, Size-dependent deformation of nanocrystalline Pt nanopillars, *Nano Lett.* **12**, 6385 (2012).
- [33] J. Rajagopalan, J. H. Han, and M. T. A. Saif, Plastic deformation recovery in freestanding nanocrystalline aluminum and gold thin films, *Science* **315**, 1831 (2007).
- [34] X. Y. Li, Y. J. Wei, W. Yang, and H. J. Gao, Competing grain-boundary- and dislocation-mediated mechanisms in plastic strain recovery in nanocrystalline aluminum, *Proc. Natl. Acad. Sci. USA* **106**, 16108 (2009).

- [35] R. G. Mariano, M. Kang, O. J. Wahab, I. J. McPherson, J. A. Rabinowitz, P. R. Unwin, and M. W. Kanan, Microstructural origin of locally enhanced CO<sub>2</sub> electroreduction activity on gold, *Nat. Mater.* **20**, 1000, (2021).
- [36] S. M. Hu, Stress-related problems in silicon technology, *J. Appl. Phys.* **70**, R53 (1991).
- [37] M. Cesar, D. P. Liu, D. Gall, and H. Guo, Calculated Resistances of Single Grain Boundaries in Copper, *Phys. Rev. Appl.* **2**, 044007 (2014).
- [38] W. D. Nix and B. M. Clemens, Crystallite coalescence: A mechanism for intrinsic tensile stresses in thin films, *J. Mater. Res.* **14**, 3467 (1999).